Nanoscale

Accepted Manuscript

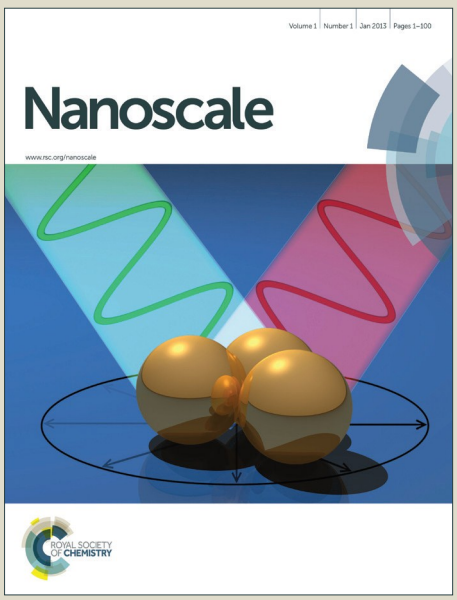

ROYAL SOCIETY OF CHEMISTRY

www.rsc.org/nanoscale

Spherical Nitrogen-doped Hollow Mesoporous Carbon as an Efficient Bifunctional Electrocatalyst for Metal-Air Batteries

Lida Hadidi†, Elaheh Davari‡, Muhammad Iqbal†, Tapas K. Purkait†, Douglas G. Ivey‡ and Jonathan G. C. Veinot*,†

†Department of Chemistry, University of Alberta, Edmonton, Alberta, Canada T6G 2G2 E-mail: jveinot@ualberta.ca

‡Department of Chemical and Materials Engineering, University of Alberta, Edmonton, Alberta, Canada T6G 2V4

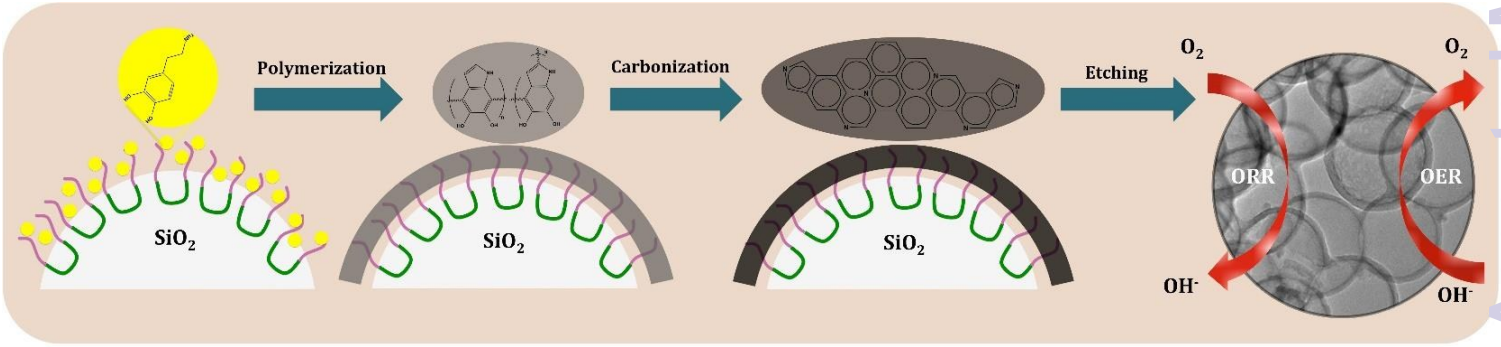

ABSTRACT

Porous carbon materials have received considerable attention as a result of their unique properties, including high surface area, high electronic conductivity, high thermal and chemical stability, low density, and availability. These characteristics make them ideal for diverse applications such as catalytic processes, sorbents for separations and gas storage, and electrode materials for batteries, fuel cells, and supercapacitors. Doping of carbon nanostructures can change the properties of these structures dramatically. In this report, dopamine has been used as the carbon precursor in the fabrication of non-metallic N-doped hollow mesoporous carbon (HMC) and these materials were tested as bifunctional electrocatalysts for oxygen reduction/evolution (ORR/OER) reactions in alkaline solutions for the first time. This cost-effective metal-free bifunctional catalyst exhibits outstanding ORR performance comparable to that of Pt-based catalysts.

1. Introduction

Recent estimates suggest fossil fuels could be depleted within the current century if the rate of population growth, energy demand, and the associated exploitation of the energy stored in fossil fuels continue unchecked.[1] Energy storage systems play key roles in energy management because they mitigate the mismatch rate between energy supply and energy demand.[2] Of the available electrical storage technologies, secondary electrochemical batteries are one of the most reliable and efficient devices. Lithium-ion batteries (LIBs) have so far dominated the market, however their low theoretical energy density (ca. 400 W h kg^{-1}) is insufficient to meet the demands of large-scale applications such as electric automobiles. Metal-air batteries such as Zn-air batteries (ZABs) offer a promising alternative boasting theoretical energy densities of up to 1084 W h kg^{-1}. ZABs generate electricity by way of redox reactions involving Zn metal and oxygen found in air.[3-5] Despite their benefits, a major hurdle for metal-air batteries is developing highly active bifunctional electrocatalysts that facilitate oxygen reduction and oxygen evolution reactions (ORR/OER) at the battery "air-breathing" cathode.[6] Currently, the most efficient ORR and OER catalysts are based upon Pt and Ir, respectively.[6] These noble metals are scarce and costly; clearly, the development of cost-effective precious metal-free bifunctional electrocatalysts is of paramount importance to the advancement and wide scale of metal-air batteries.[7-9]

Carbon is an ideal support for electrocatalysts;[10] it is electronically conductive, resistant to corrosion, straightforward to modify, easily separated from catalytic metals, abundant, and cost-effective. Many carbon systems including carbon black,[11] graphite nanofibers (GNFs) and carbon nanotubes (CNTs),[12,13] have shown promise as catalysts for ORR and oxidation of small organic molecules (e.g., alcohol and ether).[10] Despite the potential of these

promising materials, there is continued interest in the development of cost-effective durable catalysts exhibiting high activity.

Porous carbon has received substantial attention because of its abundance, high surface area, and physicochemical properties (e.g., electronic conductivity, thermal conductivity, chemical stability, and low density).[14] As a result, its potential applications are far reaching and include support materials for catalytic processes, sorbents for separation processes and gas storage, and purification, as well as electrode materials for batteries, fuel cells, and supercapacitors.[15] Porosity is one of the most important attributes of porous carbon materials because it dictates surface area and facilitates mass transport.[16] Mesoporous carbon (mC) is often preferred for electrochemical applications because of its comparatively high surface area and efficient ion mass transport.[16] Mesoporous carbon is commonly prepared using templating methods.[17-21] Soft templates such as surfactants self-assemble and guide the formation of carbon, which is generated from a subsequent carbonization reaction. Precursors have been demonstrated; examples include acetonitrile, polyvinylchloride, acetylene, anthracene, sucrose, glucose, and furfuryl alcohol, among others.[17-39]

Doping of carbon nanostructures can induce/improve favorable properties (e.g., catalytic activity, and conductivity).[40-43] Of particular note here, nanostructures of N-doped carbon frequently exhibit enhanced bifunctional catalytic activity in ORR without and with metals.[44-47] Nitrogen within carbon nanostructures influences catalytic properties because nitrogen decrease the band gap and facilitate higher electron (charge) mobility that lowers the work function at the carbon/liquid (gas) interface.[40] Doping can be achieved during synthesis (*in-situ*) or following preparation via post treatment with nitrogen-containing

species (e.g., N_2, and NH_3).[10] In the present paper, we have investigated dopamine-derived nitrogen-doped carbon as a bifunctional electrocatalyst for ORR/OER for metal-air batteries applications.

2. Results and Discussion

HMC, Silica@mC, and PDA beads were prepared using straightforward dopamine polymerization followed by carbonization. The resulting structures were fully characterized and evaluated as bifunctional electrocatalysts in alkaline solutions. Stöber silica particles, used in the present study as templates in the formation of Silica@mC were prepared by exploiting standard sol-gel processing. As-synthesized Stöber silica particles (diameter = 170 nm ± 10%) were coated with dopamine and triblock copolymer PEO-PPO-PEO (F127); this layer was oxidatively polymerized under basic conditions.[50] Finally, the polymer layer was carbonized upon heating in Ar at 400 °C for 2 h and at 800 °C for 3 h.

Fig. 1 shows representative electron microscopy images of coated Stöber silica particles before and after carbonization. After heating at 800 °C (Fig. 1B and 1D) the general shell structure and spherical shape remain. The shell thickness after carbonization is ca. 21 nm ± 28%. Etching with alcoholic hydrofluoric acid provided a convenient method for removing the silica template. Consistent with a porous structure (*vide infra*), one hour of etching provided hollow uniformly shaped hollow mesoporous spheres bearing no evidence (using TEM, SEM, EDX, and XPS techniques) (Fig. S1 and S2†) of silica.

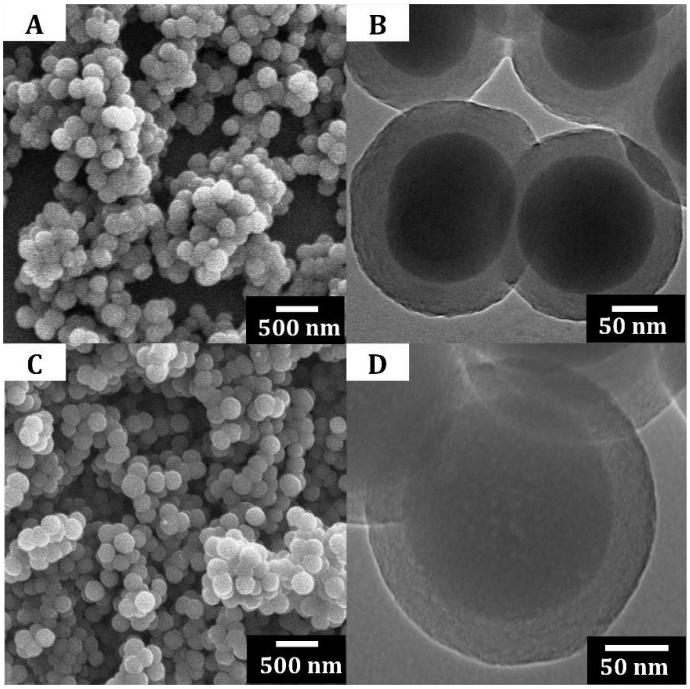

Fig. 1. Secondary electron SEM images of coated silica before (A) and after (C) carbonization. Bright field TEM images of carbon-coated silica before (B) and after (D) carbonization.

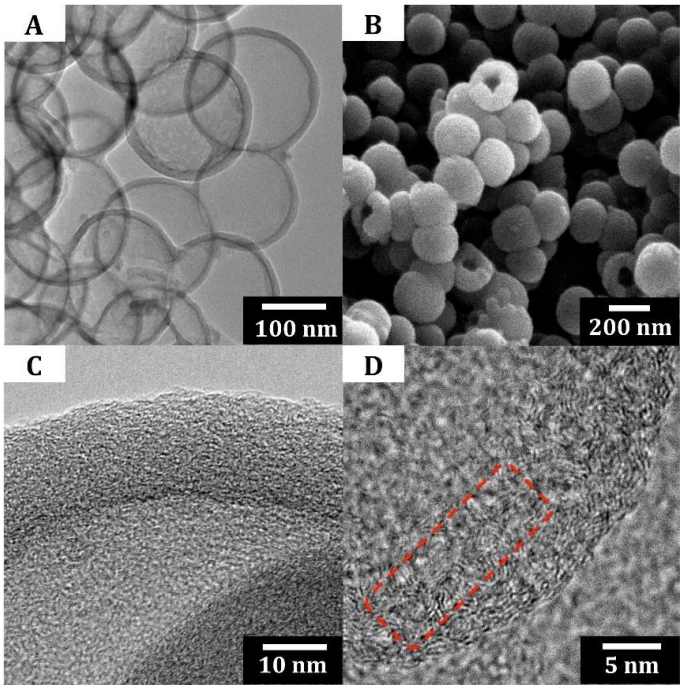

Fig. 2. (A) Bright field TEM image of HMC. (B) Secondary electron SEM image of HMC. (C) and (D) HR-TEM images of HMC.

Evaluation of the carbon shells using HR-TEM revealed graphitic (Fig. 2D) and amorphous domains. PDA beads (d = 121 μm ± 28%; Fig. S3†) were also prepared via oxidative polymerization of dopamine in a Tris-HCl buffer solution.[50,51] Carbonization was achieved using the same conditions used for HMC (*vide supra*). The present carbonaceous materials were further characterized using XPS, FTIR, and Raman spectroscopy. The survey XP spectrum showed the materials consisted of only carbon, nitrogen, and oxygen, as well as trace silicon (Fig. S2†). No evidence of metals was detected at the sensitivity of the XPS method. The N1s XPS spectra provide insight into the environment of the N atoms in Silica@mC, HMC, and PDA beads. In Fig. 3 we show typical spectra for Silica@mC and HMC with peak deconvolution that suggests two components centered at 398.2 and 400.3 eV, corresponding to pyridinic N and pyrrolic N, respectively. Similar analysis of PDA beads shows pyrrolic N with only minor contributions from pyridinic N approaching the sensitivity limits of the XPS method. Speciation of the nitrogen content in Silica@mC, HMC, and PDA beads is summarized in Table 1.

Table 1. Relative atomic ratios of nitrogen species for HMC, Silica@mC, and PDA beads

Catalyst	N content (at%)	Pyridinic N (at %)	Pyrrolic N (at%)
HMC	7.08	0.58	6.5
Silica@mC	4.34	0.56	3.8
PDA beads	4.9	0.08	4.81

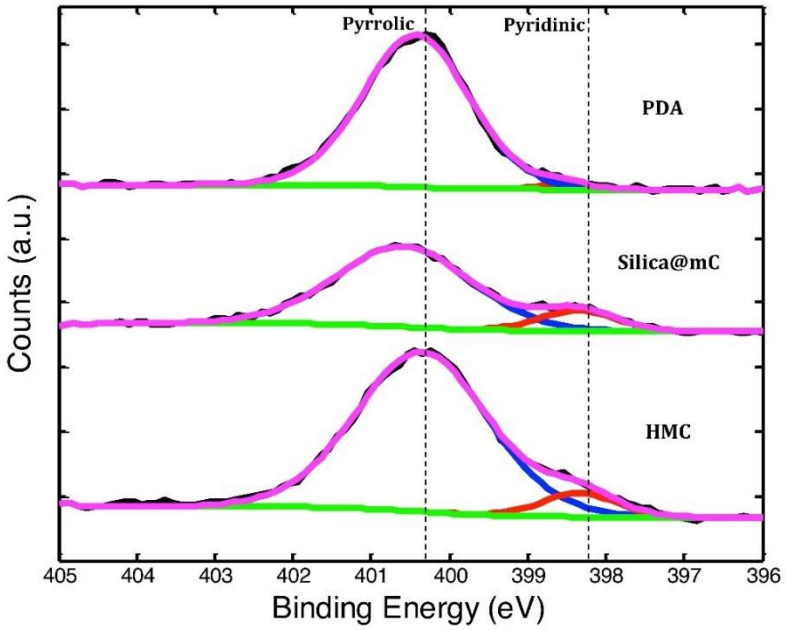

Fig. 3. Representative high-resolution XPS spectra of N1s for PDA beads, Silica@mC, and HMC.

FTIR spectra of PDA beads, Silica@mC, and HMC are shown in Fig. 4. The PDA beads spectrum shows absorption at 2921 cm^{-1}, which is confidently assigned to C-H stretching modes and a feature at 1431 cm^{-1} arising from heterocyclic stretching (C-N bonds).[50] The peak at 1161 cm^{-1} is the result of heterocyclic N-H in-plane deformation breathing.[50] In addition, a feature associated with C-N bending is found at ca. 1500 cm^{-1} and appears to be merged with the heterocyclic stretching feature at 1431 cm^{-1}.[50] The IR spectrum of Silica@mC shows a strong band at 1103 cm^{-1}, which is assigned to the Si-O-Si stretching mode. As expected this feature is not obvious after HF etching (HMC). A feature associated with C-N bending is observed for Silica@mC and HMC at ca. 1570 cm^{-1}.

The Raman spectra for Silica@mC, HMC, and PDA beads (Fig. 5) show two features are at 1331 and 1578 cm^{-1} that corresponds to the D band and G band, respectively. The D band

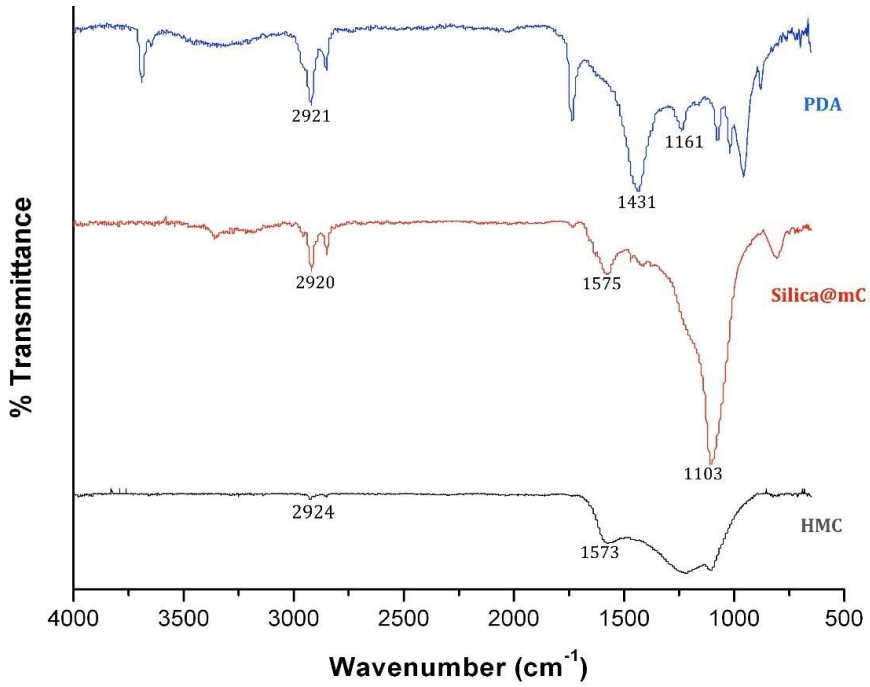

Fig. 4. FTIR spectra for PDA beads, Silica@mC, and HMC.

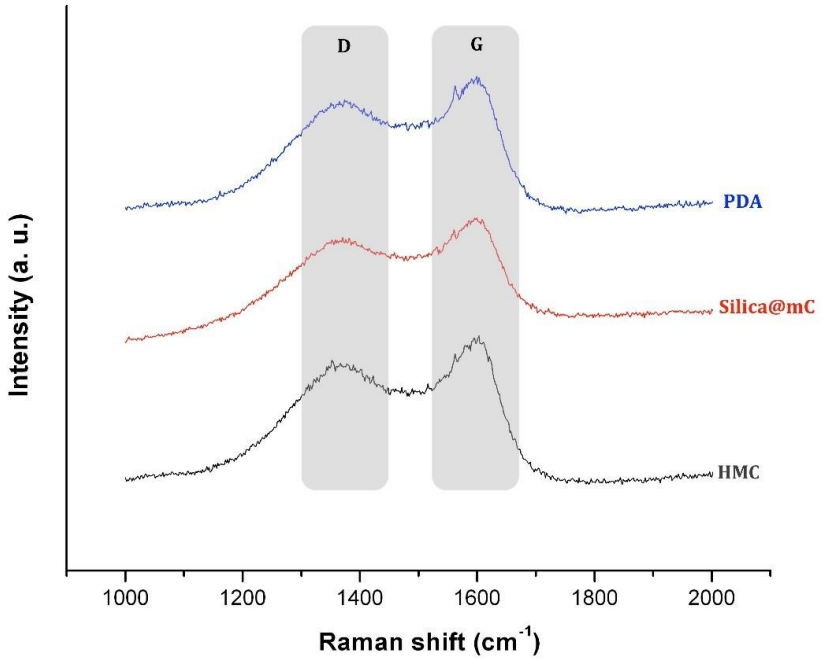

Fig. 5. Raman spectra for PDA beads, Silica@mC, and HMC.

arises from the A_{1g} breathing mode arising from sp^3 carbon components, while the G peak corresponds to in-plane stretching of bonds involving sp^2 carbon atoms.[50] Based upon

these observations and the HR-TEM data (*vide supra*), we conclude all the present materials contain a mixture of graphitic and amorphous carbon.

Nitrogen sorption analysis was used to evaluate the specific surface area, pore volume, and average pore diameter of the Silica@mC, HMC, and PDA beads. The corresponding isotherms (Figs. S4, S5, and S6†) show a distinct hysteresis loop at high relative pressure consistent with mesoporous materials as defined by IUPAC.[49] Analysis of HMC indicates it possesses porosity consisting of uniformly sized mesopores (ca. 30 nm). The Silica@mC and PDA beads show pore sizes of about 50 nm and 10 nm, respectively. Of the three materials, HMC exhibits the highest BET surface area (i.e., 340 m^2/g) and pore volume (2.5 cm^3/g) followed by Silica@mC and then PDA beads.

Table 2. Textural properties of HMC, Silica@mC, and PDA beads

Catalyst	BET surface area (m^2/g)	Pore diameter (nm)	Pore volume (cm^3/g)
HMC	340	30	2.5
Silica@mC	22	50	0.28
PDA beads	45	10	0.1

cyclic voltammogram for HMC (Fig. 6) shows a featureless capacitive current in the Ar- The ORR catalytic activity of HMC was explored using a conventional three-electrode system within Ar or O_2-saturated 0.1 M KOH as the electrolyte. Cyclic voltammetry (CV) experiments were performed after removal of dissolved oxygen from the solution. The saturated electrolyte. After purging the electrolyte solution with O_2, an irreversible cathodic current at -0.17 V indicative of ORR occurring at the HMC surface appears.

The ORR catalytic activity of HMC was explored using a conventional three-electrode system within Ar or O_2-saturated 0.1 M KOH as the electrolyte. Cyclic voltammetry (CV) experiments were performed after removal of dissolved oxygen from the solution. The cyclic voltammogram for HMC (Fig. 6) shows a featureless capacitive current in the Ar-saturated electrolyte. After purging the electrolyte solution with O_2, an irreversible cathodic current at -0.086 V indicative of ORR occurring at the HMC surface appears.

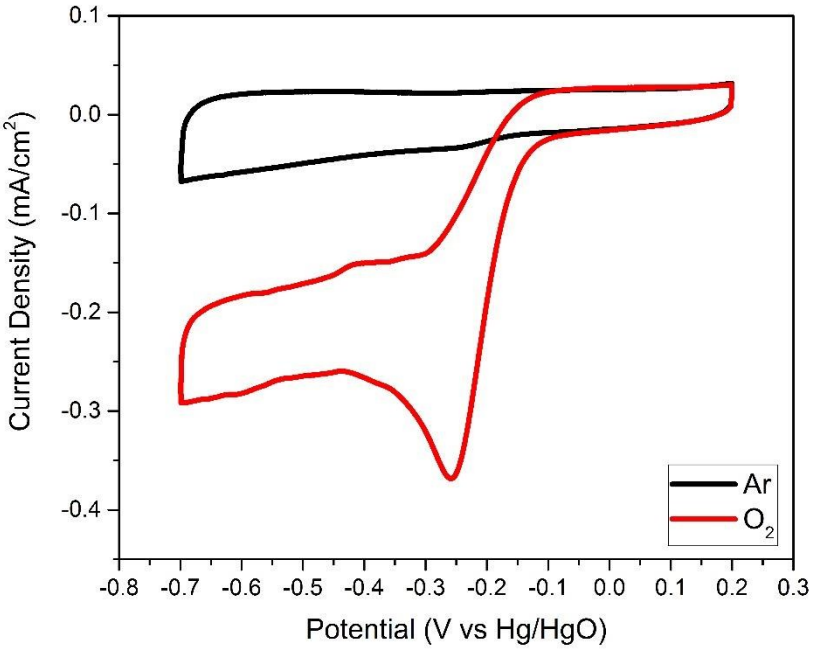

Fig. 6. Cyclic voltammograms for HMC in Ar (black trace) and O_2 (red trace) in saturated 0.1 M KOH with a scan rate of 10 mV s^{-1}.

To evaluate the ORR performance of the HMC, LSV was conducted from -0.8 to 0.1 V vs. Hg/HgO using predefined electrode rotation rates (400, 900, 1600 and 2500 rpm) and a scan rate of 10 mV s^{-1} in O_2-saturated 0.1 M KOH solution (Fig. 7A). The results for Silica@mC and PDA beads are shown in Fig. S7 and S8†.

The ORR polarization curve for HMC can be divided into three regions: i) kinetically controlled (ca. -0.1 to -0.3 V), ii) kinetic-diffusion controlled (ca. -0.3 to -0.6 V), and iii) mass diffusion controlled (less than -0.6V) (Fig. 7A). ORR is commonly evaluated using Koutecky-Levich (K-L) plots (Fig. 7B).[52] The overall current density can be separated into diffusion and kinetic currents by applying K-L equations noted below:[53]

$$\frac{1}{j} = \frac{1}{j_k} + \frac{1}{j_l} = \frac{1}{Bw^{1/2}} + \frac{1}{j_k} \qquad (1)$$

$$B = 0.62nFC_o(D_o)^{2/3}\eta^{-1/6} \qquad (2)$$

$$j_k = nFKC_o \qquad (3)$$

where, j, j_l, and j_k are the measured, kinetic, and diffusion-limiting current densities, respectively, ω is the angular velocity of the electrode ($\omega = 2\pi N$, N is the linear rotation), n is the number of electrons transferred during ORR, F is the Faraday constant ($F = 96485\ Cmol^{-1}$), C_o is the bulk concentration of O_2 ($C_o = 1.2 \times 10^{-3}\ molL^{-1}$), D_o is the diffusion coefficient of O_2 in the KOH electrolyte ($D_o = 1.9 \times 10^{-5}\ cm^2s^{-1}$) , υ is the kinematic viscosity of the electrolyte ($\upsilon = 0.01\ cm^2s^{-1}$ in 0.1 M KOH), and k is the electron-transfer rate constant. The limiting current density increases with oxygen flux to the electrode surface. Consistent with first-order kinetics of ORR with respect to the concentration of dissolved O_2 the K-L plots for HMC (Fig. 7) show linear relationships for I^{-1} as a function of $(\omega)^{-1/2}$. The non-zero intercept shows that O_2 reduction is under diffusion-kinetic control.

Oxidation-reduction in alkaline solutions proceeds by a direct two-electron (Eqs. 4 and 5) or a four-electron pathway (Eq. 6)[52],

$$O_2 + 2H_2O + 2e^- \longrightarrow HO_2^- + OH^- \quad (4)$$

$$2HO_2^- \longrightarrow 2OH^- + O_2 \quad (5)$$

$$O_2 + 2H_2O + 4e^- \longrightarrow 4OH^- \quad (6)$$

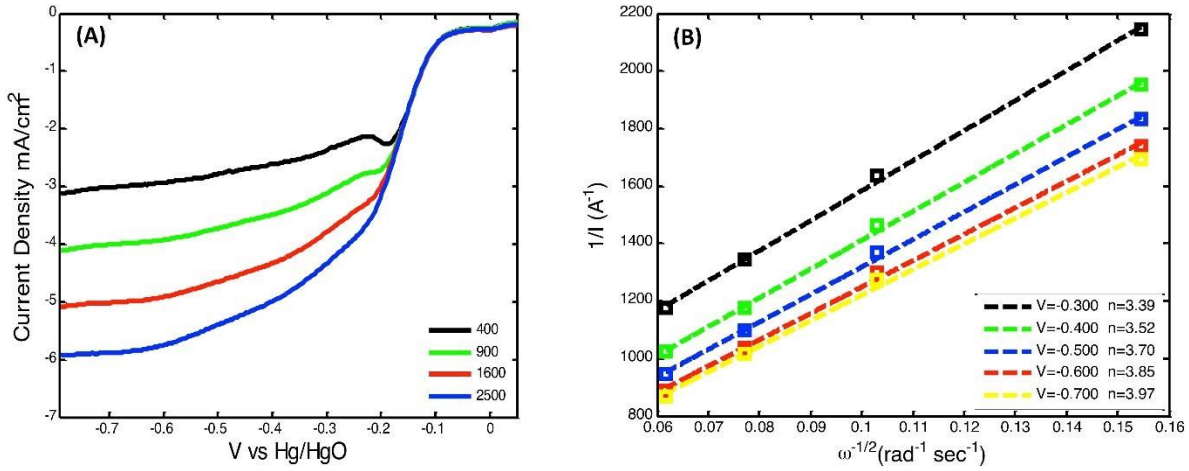

Fig. 7. (A) ORR LSV curves for HMC in an O_2-saturated 0.1 M KOH solution at indicated rotational rates and a scan rate of 10 mV s^{-1}. (B) Koutecky-Levich plots for HMC in the potential range of -0.3 to -0.7 V vs. Hg/HgO.

Applying the K-L relationships to the present systems yields the number of electrons transferred as ca. 4 for the potentials investigated and the number increases at more negative potentials, which indicates the further reduction of hydrogen peroxide (Eq. 6) to hydroxide in this potential range. These results indicate the electrocatalytic process of HMC proceeds via the four-electron mechanism and is appropriate for ORR.[54]

The ORR LSVs of the candidate catalysts obtained at 1600 rpm are shown in Fig. 8A. The catalysts were initially cycled 40 times at 10 mV s^{-1} in 0.1 M KOH O_2-saturatd solution in order to stabilize the catalyst. Comparing the response of the catalysts, HMC shows the highest ORR kinetic-limiting current density (ca. -4.9 mA cm^{-2}) of the carbon-based catalysts investigated. This value exceeds the current density for Pt/C (ca. -4.4 mA cm^{-2}), which is the benchmark catalyst for ORR. The ORR onset potential for HMC (ca. -0.076 V) is

the most positive of the catalysts studied in this work and is ca. 76 mV more negative than the ORR onset potential for commercial 40% Pt/C (ca. 0.0004V). The ORR activity of the HMC particles is comparable to that of other mesoporous carbons, but the current density of the present system is higher.[55] The half-wave potential ($E_{1/2}$) (the potential where the current density reaches half the limiting current), provides insight into the capability of catalysts to decrease the ORR overpotential. The $E_{1/2}$ for HMC is only 170 mV more negative than that of 40% Pt/C. From this data, we conclude that HMC exhibits excellent electrocatalytic activity.

The catalytic activity of cycled HMC for OER was tested using LSV. Fig. 8B shows a large anodic current due to the oxidation of water. Clearly the OER activity of the present HMC is superior to that of the other carbon-based materials and the 40% Pt/C material.

Table 3 summarizes the bifunctional oxygen activity of HMC, Silica@mC, and PDA beads. To assess the overall oxygen catalytic activity, the difference between ORR and OER onset potentials was tabulated. A smaller difference indicates better catalytic behavior for the bifunctional electrode. Based upon this metric, HMC particles have an onset potential difference of 0.35 V, which compares favorably to precious metals.[56]

ORR-OER bifunctional catalytic activity depends upon the surface area and nitrogen content of the structure.[57] According to the data summarized in Table 1, HMC has the highest nitrogen content of the samples investigated. The nitrogen bonding environment (e.g., pyridinic, pyrrolic, and graphitic) influences catalytic activity; the literature suggests that proportion of pyridinic and pyrrolic nitrogen play key roles.[56-60] Still, conflicting reports exist regarding the precise relationship between catalytic activity and nitrogen speciation.[58] Comparison of HMC, Silica@mC, and PDA beads shows differences in specific

surface area, pore size, pore volume, and nitrogen speciation. The specific surface area of HMC is the highest (340 $m^2 g^{-1}$) of the studied structures (Table 1).

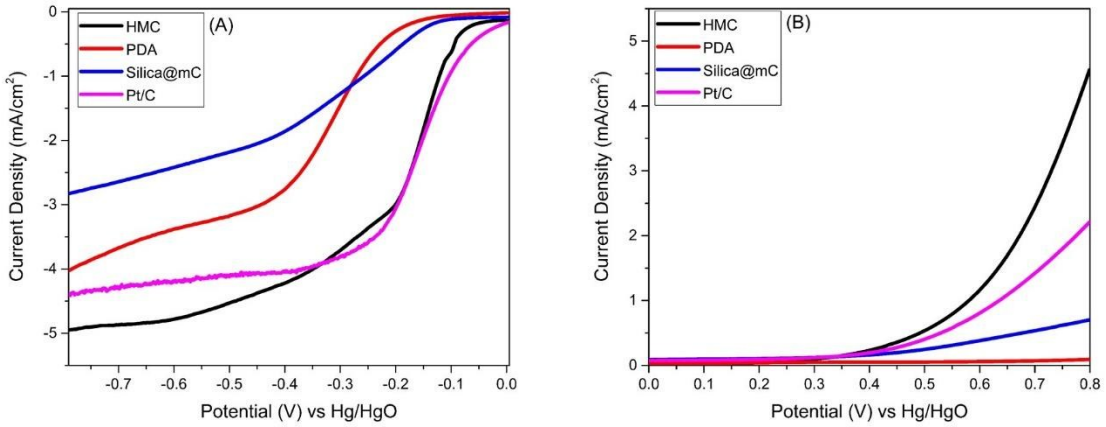

Fig. 8. (A) ORR LSV curves for HMC, Silica@mC, PDA beads, and Pt/C in an O_2-saturated 0.1 M KOH solution at 1600 rpm. (B) OER LSV curves for HMC, Silica@mC, PDA beads, and Pt/C in 0.1 M KOH solution at 1600 rpm.

Table 3. Oxygen electrode catalyst activities

Catalyst	ORR onset (V)	ORR $E_{1/2}$ (V)	j_l ($mAcm^{2-}$)	n at -0.7V	OER onset (V)	E_{OER}-E_{ORR} (V)
HMC	-0.055	-0.17	-4.95	3.97	0.17	0.35
Silica@mC	-0.112	-0.33	-2.85	2.83	0.2	0.53
PDA beads	-0.165	-0.33	-4.05	3.47	0.4	0.73
Pt/C	0.0004	-0.16	-4.39	4	0.21	0.37

i_l: limiting current density
n: number of electrons transferred
$E_{½}$: half-wave potential

Furthermore, the pore volume of HMC particles is an order of magnitude higher than that of both Silica@mC and PDA beads, which is consistent with the electrochemical performance of HMC. The mesoporous nature of HMC provides more active sites for ORR and OER. These factors along with the type of nitrogen doping contribute to the different

electrochemical performances. Therefore, the synergistic effect of high surface area and nitrogen doping improve the bifunctional electrocatalytic activity of HMC.

The short-term durability of HMC was evaluated by chronoamperometry at a constant potential of -0.2 V vs. Hg/HgO for 3 h in O_2-staurated 0.1 M KOH at 1600 rpm. The chronoamperometric results are shown in Fig. 9. The HMC catalyst exhibits higher relative current over time than 40% Pt/C. After 3 h, 40% Pt/C retained 54.7% of the initial current, whereas HMC retained 70.1% of its initial current. This shows the good stability of the HMC in addition to its promising bifunctional activity. The gradual decay of the reduction current may be due to insufficient gas flux or slow catalyst removal from the electrode surface during testing. Activity degradation of 40% Pt/C catalysts in alkaline solutions has been observed previously and has been attributed to the dissolution or aggregation of Pt nanoparticles.[6]

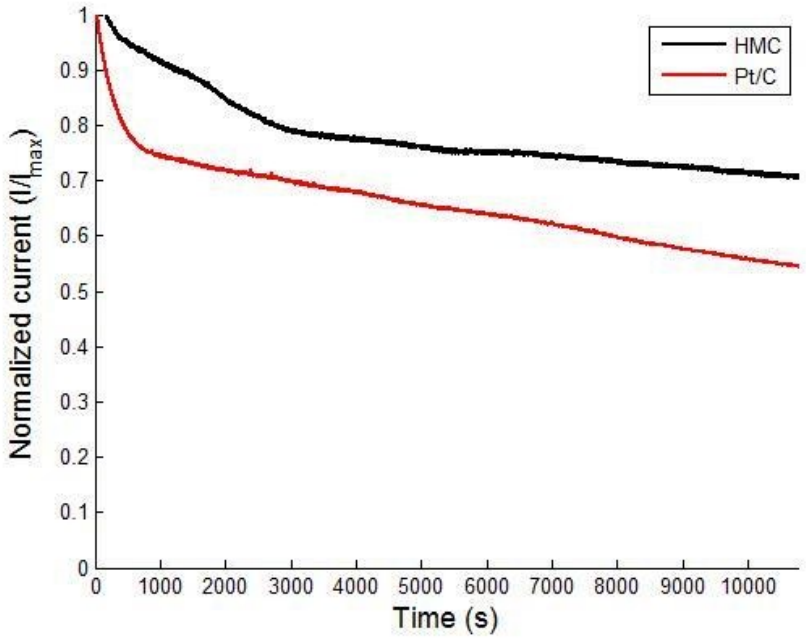

Fig. 9. Chronoamperometric responses for ORR for HMC and Pt/C catalysts at -0.2 V vs. Hg/HgO in O_2-saturated 0.1 m KOH solution at a rotational rate of 1600 rpm.

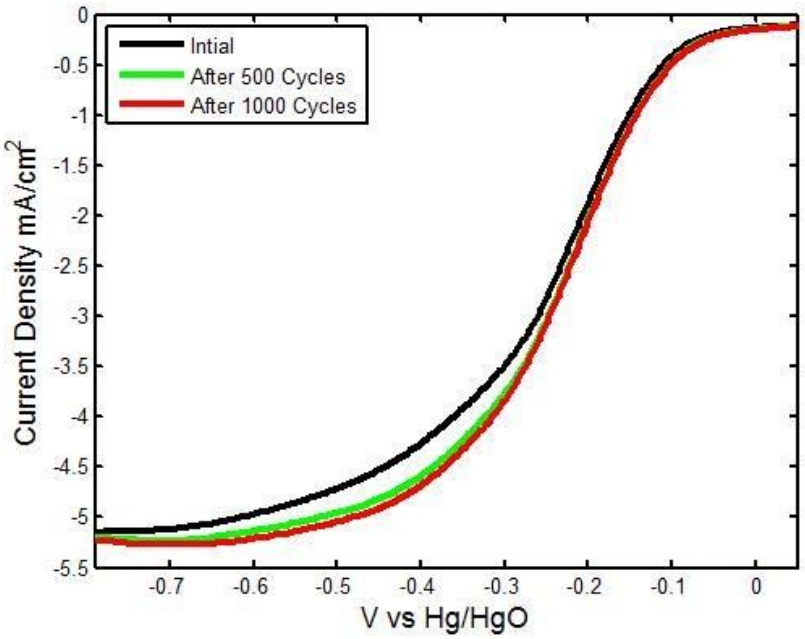

Fig. 10. LSV ORR curves measured during cycling of HMC in O_2-saturated 0.1 M KOH at 1600 rpm (potential range -0.8-0.35 V vs. Hg/HgO at 100 mV s^{-1}).

The relatively good stability of HMC was confirmed by extended cycling of the catalysts. This is shown in Fig. 10 where HMC has been exposed to repeated potential cycles from -0.8 to 0.7 V vs. Hg/HgO in O_2-saturated electrolyte at 100 mV s^{-1}. After 1000 cycles, only minimal changes to ORR kinetics are observed. In fact there is a slight increase in the magnitude of the current density with cycling. The good stability is attributed to the nature of HMC active sites, which are nitrogen doped, and the corrosion resistance nature of the HMC particles. The high stability and rapid kinetics may arise from the high surface area and multiple active sites for oxygen adsorption.[61]

3. Conclusions

The synthesis and characterization of N-doped carbon mesostructures obtained from the carbonization of polymerized dopamine have been reported. Hollow mesoporous carbon (HMC) exhibits high oxygen reduction reaction (ORR) and oxygen evolution reaction (OER)

activity and superior stability in alkaline electrolytes compared with baseline Pt/C catalysts. The unique structures of the porous shell provide abundant active sites for oxygen adsorption and desorption and facilitate the diffusion of reactants during the catalytic processes. The small pore size and nitrogen doped active sites boost the diffusion-limiting current and long-term stability. As a result, HMC is a promising high performance alternative to precious metal bifunctional catalysts in Zn-air battery applications.

4. Experimental Section

Materials. Dopamine hydrochloride, pluronic F127, tris-(hydroxymethyl) amino-methane, hexadecyltrimethylammonium bromide (CTAB) (≥99%), and tetraethoxysilane (TEOS) (≥99%) were purchased from Sigma-Aldrich and used as received. Pt/C (40%), Nafion solution (5% w/w in water), and 1-propanol (99.99%) were purchased from Alfa Aesar. Potassium hydroxide was purchased from Fisher and used as received.

Preparation of Stöber Silica Spheres. Spherical silica particles were prepared using the Stöber method and tetraethoxysilane (TEOS) as the silica source as previously reported.[48] For a typical synthesis 40 mL of 0.2 M TEOS was added to a mixed solution of 50% ethanol (80 mL) and ammonium hydroxide (28%, 4 mL) and then stirred for 3 hours at ambient temperature. The solution was centrifuged three times at a speed of 10000 rpm for 30 min to collect the particles.

Synthesis of Silica@mC Particles. For a typical synthesis 15 mg of Stöber silica (170 ± 10%), 7.5 mg of triblock copolymer pluronic F127 and 4.5 mg of 2-amino-2-hydroxymethyl-propane-1,3-diol (tris) were dispersed/dissolved in 4 mL of deionized water. Subsequently, dopamine hydrochloride (15 mg) was added and the mixture was stirred at room temperature for 24 hours. The resulting polydopamine coated silica

particles were collected by centrifugation at a speed of 10000 rpm for half an hour. The particles were washed three times using ethanol (25 mL), and then dried under vacuum. The resulting white powder was placed in a quartz boat in a tube furnace and heated to 400 ˚C (heating rate of 1 ˚C/min) and held for 2 h. The temperature was then raised (heating rate of 5 ˚C/min) to 800 ˚C and held for 3 h; this was followed by cooling to room temperature.[49] All heating and cooling was performed under a flowing Ar atmosphere.

Synthesis of Hollow Mesoporous Carbon Particles (HMC). As-synthesized silica@mC particles (ca. 0.2 g) were placed in a PET beaker. Water (2 mL), ethanol (2 mL), and aqueous 49% HF (2 mL) were subsequently added sequentially and the mixture was stirred for 1 h at room temperature. The particles were recovered via vacuum filtration and washed with water (60 mL) and ethanol (60 mL). The resulting black powder was finally dried under vacuum. The HMC product (0.05 mg) was characterized using transmission and scanning electron microscopy (TEM and SEM), Raman and infrared (IR) spectroscopy, X-ray photoelectron spectroscopy (XPS), nitrogen adsorption/desorption measurements.

Preparation of Polydopamine Beads (PDA). Dopamine (0.3 mg/mL) was dissolved in Tris-HCl buffer (10 mM and pH=8.8) and the resulting solution was stirred for 12 hours.[50] The black suspension was centrifuged at 14000 rpm for 30 min. The clear supernatant was decanted and discarded. The black precipitate was washed three times in water (60 mL) with sonication followed by recovery by centrifugation. Finally, the sample was dried under vacuum and heated in an Ar atmosphere in a tube furnace, as outlined for the Silica@mC particles (*vide supra*).

Electrochemical measurements. All electrochemical measurements were performed using a Bio-Logic SP-300 potentiostat/galvanostat. Linear sweep voltammetry (LSV) half-

cell experiments were performed using a rotating disc electrode (RDE) (Pine Instruments Co, AFMSRCE). A three-electrode cell configuration was employed with a catalyst coated glassy carbon (5 mm diameter) working electrode, Pt coil counter electrode, and Hg/HgO (1 M NaOH, 0.098 V vs. NHE at 25 °C) reference electrode. The electrolyte used for all measurements was a 0.1 M KOH aqueous solution. A catalyst ink was prepared by ultrasonic mixing of 20 mg of the catalyst of choice, 2 ml of 5% Nafion solution (5% w/w in water and 1-propanol dispersion, ≥ 0.92 meq/g exchange capacity), and 1-propanol or 30 minutes. A 5 μL aliquot of ink was drop coated on a glassy carbon disc and dried in air to yield a film with catalyst loading of 0.10 mg cm^{-2}. Cyclic voltammetry (CV) was performed at a scan rate of 10 mV s^{-1} in Ar and O_2 saturated electrolytes. The Ar saturated electrolyte was prepared by purging a 0.1 M KOH aqueous solution with high purity (i.e., >99.99%) Ar for 20 minutes. After testing, the solution was purged with O_2 (>99.5%) for 10 minutes at a constant flow. LSV curves were obtained using a rotating working electrode at predefined rotation rates (400, 900, 1600, and 2500 rpm) and a scan rate of 10 mV s^{-1}.

Material Characterization

Fourier-Transform Infrared Spectroscopy (FT-IR). FT-IR was performed on a Nicolet Magna 750 IR spectrometer by drop coating an ethanol dispersion of particles on a piece of silicon wafer.

Electron Microscopy (EM). Transmission electron microscopy was performed using a JEOL 2010 TEM equipped with a LaB_6 thermionic emission filament operated at an accelerating voltage of 200 kV. Samples for TEM analysis were prepared by placing a drop of a dilute ethanol suspension of the material of interest onto a carbon-coated, 200-mesh Cu grid and drying at room temperature.

High-resolution (HR) TEM images were acquired using a Hitachi-9500 TEM operated at an accelerating voltage of 300 kV and processed using Gatan ImageJ software (Version 1.48v). Samples were prepared by drop casting dilute ethanol suspensions of the sample of choice onto a holey carbon-coated copper grid (400 mesh).

Scanning electron microscopy (SEM) was carried out with a JEOL 6301F field emission SEM operated at an acceleration voltage of 5 kV. Samples were prepared by drop casting samples of choice from dilute ethanol suspensions onto a clean Si (100) wafer.

X-ray Photoelectron Spectroscopy (XPS). XPS was performed using a Kratos Axis Ultra instrument with a monochromatic Al Kα source (λ = 8.34 Å) with an energy hν = 1486.6 eV. Survey spectra were collected with analyzer pass energy of 160 eV and a step of 0.3 eV. For high-resolution spectra, the pass energy was 20 eV and the step was 0.1 eV with dwell time of 200 ms. The base pressure in the sample analytical chamber was lower than 1×10^{-9} torr. Binding energies were calibrated by using the carbon 1s peak as a reference (284.6 eV). CASA XPS version 2.3.13 was used to accomplish the background subtraction and curve fitting.

Nitrogen Adsorption Porosimetry. Nitrogen adsorption-desorption isotherms were measured at -196 ˚C with a Quantachrome Autosorb-1 adsorption analyzer. Prior to adsorption measurements, samples were degassed at 250 ˚C under vacuum for 2 h. The data were analyzed using Brunauer-Emmett-Teller (BET) theory. The specific surface area was determined from the linear portion of the BET equation and the total pore volume was calculated from the amount adsorbed at a relative pressure of about P/P_o=0.995. The pore size distributions (PSDs) were obtained using Density Functional Theory (DFT).

Raman Spectroscopy. Raman spectra of the particles were measured with a Renishaw inVia Raman microscope. The excitation wavelength was 514 nm. Samples were prepared by mounting the powder on aluminum foil.

Acknowledgments

The authors recognize NSERC and the Canada Foundation for Innovation (CFI) for continued generous support. The following people and organization are gratefully acknowledged as well: C. W. Moffat for FT-IR measurements, D. Karpuzov and the staff at the Alberta Centre for Surface Engineering and Science (ACSES) for XPS analysis, K. Kui for HRTEM imaging, A. Y. Mahmoud for Raman measurements, and the University of Alberta nanoFAB. M. Javadi and the members of the Veinot research team are also thanked for useful discussion.

References:

1 Osaka. T.; Ogumi, Z. *Nanoscale Technology for Advanced Lithium Batteries*; Springer: London, 2014.

2 Linden, D.; Reddy, T. B. *Linden's Handbook of Batteries*, Fourth.; McGraw-Hill: New York, 2011.

3 Cheng, F.; Chen, J. *Chem. Soc. Rev.* **2012**, *41* (6), 2172–2192.

4 Li, Y.; Dai, H. *Chem. Soc. Rev.* **2014**, *43* (15), 5257–5275.

5 Beck, F.; Rüetschi, P. *Electrochim. Acta* **2000**, *45* (15-16), 2467–2482.

6 Cheng, F.; Chen, J. *Chem. Soc. Rev.* **2012**, *41* (6), 2172–2192.

7 Neburchilov, V.; Wang, H.; Martin, J. J.; Qu, W. *J. Power Sources* **2010**, *195* (5), 1271–1291.

8 Lee, J.-S.; Kim, S. T.; Cao, R.; Choi, N.-S.; Liu, M.; Lee, K. T.; Cho, J. *Adv. Energy Mater.* **2011**, *1* (1), 34–50.

9 Jörissen, L. *J. Power Sources* **2006**, *155* (1), 23–32.

10 Shao, Y.; Sui, J.; Yin, G.; Gao, Y. *Appl. Catal. B Environ.* **2008**, *79* (1), 89–99.

11 Xu, X.; Tan, C.; Liu, H.; Wang, F.; Li, Z.; Liu, J.; Ji, J. *J. Electroanal. Chem.* **2013**, *696*, 9–14.

12 Serp, P. *Appl. Catal. A Gen.* **2003**, *253* (2), 337–358.

13 Lee, K.; Zhang, J.; Wang, H.; Wilkinson, D. P. *J. Appl. Electrochem.* **2006**, *36* (5), 507–522.

14 Liang, C.; Li, Z.; Dai, S. *Angew. Chem. Int. Ed. Engl.* **2008**, *47* (20), 3696–3717.

15 Lin, C. F.; Zhang, X.; Lin, H.; Wang, N.; Li, J. B.; Yang, X. Z. *Adv. Mater. Res.* **2006**, *11-12*, 543–546.

16 Chen, X.; , Kierzek, K. *J. Phys. Chem. C* **2011**, *115*, 17717-17724.

17 Tanaka, S.; Nishiyama, N.; Egashira, Y.; Ueyama, K. *Chem. Commun. (Camb).* **2005**, 16, 2125–2127.

18 Knox, J. H.; Unger, K. K.; Mueller, H. *J. Liq. Chromatogr.* **2006**, *6* (sup001), 1–36.

19 Liang, C.; Hong, K.; Guiochon, G. a; Mays, J. W.; Dai, S. *Angew. Chem. Int. Ed. Engl.* **2004**, *43*, 5785–5789.

20 Knox, H.; Kaur, B. *J. Liq. Chromatogr*. **1986**, *352*, 3–25.

21 Liang, C.; Dai, S. *J. Am. Chem. Soc.* **2006**, *128*, 5316–5317.

22 Ryoo, B. R.; Joo, S. H.; Kruk, M.; Jaroniec, M. *Adv. Mater*. **2001**, *13* (9), 677–681.

23 Zhang, B. W.; Liang, C.; Sun, H. *Adv. Mater*. **2002**, *14* (23), 1776–1778.

24 Meng, Y.; Gu, D.; Zhang, F.; Shi, Y.; Cheng, L.; Feng, D.; Wu, Z.; Chen, Z.; Wan, Y.; Stein, A.; Zhao, D. *Chem. Mater*. **2006**, *18* (4), 4447–4464.

25 Kim, T.-W.; Park, I.-S.; Ryoo, R. *Angew. Chem. Int. Ed. Engl.* **2003**, *42* (36), 4375–4379.

26 Lee, B. J.; Yoon, S.; Oh, S. M. *Adv. Mater*. **2000**, *12* (5), 359–362.

27 Vix-guterl, C.; Parmentier, J.; Werckmann, J. *Chem. Lett*. **2002**, *31* (10), 1062–1063.

28 Kyotani, T.; Tomita, A. *Chem. Mater*. **1995**, *7* (8), 1994–1995.

29 Xia, Y.; Mokaya, R. *Chem. Mater*. **2005**, *17* (6), 1553–1560.

30 Kim, C. H.; Lee, D.; Pinnavaia, T. J. *Langmuir* **2004**, *20* (13), 5157–5159.

31 Li, Z.; Jaroniec, M.; Lee, Y.; Radovic, L. R. *Chem. Commun*. **2002**, 1346–1347.

32 Oda, Y.; Fukuyama, K.; Nishikawa, K.; Namba, S.; Yoshitake, H.; Tatsumi, T. *Chem. Mater*. **2004**, *16* (20), 3860–3866.

33 Rodriguez, A. T.; Chen, M.; Chen, Z.; Brinker, C. J.; Fan, H. *J. Am. Chem. Soc*. **2006**, *128*, 9276–9277.

34 Kim, S.-S.; Pauly, T. R.; Pinnavaia, T. J. *Chem. Commun.* **2000**, *123* (17), 1661–1662.

35 Kaneda, M.; Tsubakiyama, T.; Carlsson, A.; Sakamoto, Y. *J. Phys. Chem. B* **2002**, *106* (6), 1256–1266.

36 Li, Z.; Jaroniec, M. *Chem. Mater*. **2003**, *15*, 1327–1333.

37 Lee, J.; Yoon, S.; Hyeon, T.; Oh, M.; Bum, K. *Chem. Commun*. **1999**, 2177–2178.

38 Ryoo, R.; Joo, S. H.; Jun, S. *J. Chem. Phys. B* **1999**, *103* (37), 7743-7746.

39 Lin, H.-P.; Chang-Chien, C.-Y.; Tang, C.-Y.; Lin, C.-Y. *Microporous Mesoporous Mater.* **2006**, *93* (1-3), 344–348.

40 Strelko, V. V; Kuts, V. S.; Thrower, P. A. *Carbon* **2000**, *38*, 1499–1503.

41 Terrones, M. *Annu. Rev. Mater. Res.* **2003**, *33* (1), 419–501.

42 Terrones, B. M.; Redlich, P.; Grobert, N.; Trasobares, S.; Hsu, W.; Terrones, H.; Zhu, Y.; Hare, J. P.; Reeves, C. L.; Cheetham, A. K.; Rühle, M.; Kroto, H. W.; Walton, D. R. M. *Adv. Mater.* **1999**, *11* (8), 655–658.

43 Fuertes, A. B.; Alvarez, S. *Carbon N. Y.* **2004**, *42* (15), 3049–3055.

44 Sidik, R. A.; Anderson, A. B.; Subramanian, N. P.; Kumaraguru, S. P.; Popov, B. N. *J. Phys. Chem. B* **2006**, *110*, 1787–1793.

45 Sun, C.; Chen, L.; Su, M.; Hong, L.; Chyan, O.; Hsu, C.; Chen, K.; Chang, T.; Chang, L. *Chem. Mater.* **2005**, *17* (14), 3749–3753.

46 Matter, P.; Zhang, L.; Ozkan, U. *J. Catal.* **2006**, *239* (1), 83–96.

47 Lei, C.; Han, F.; Li, D.; Li, W.-C.; Sun, Q.; Zhang, X.-Q.; Lu, A.-H. *Nanoscale* **2013**, *5*, 1168-1175.

48 Dasog, M.; Smith, L. F.; Purkait, T. K.; Veinot, J. G. C. *Chem. Commun. (Camb).* **2013**, *49* (62), 7004–7006.

49 Ru, Y.; Evans, D. G.; Zhu, H.; Yang, W. *RSC Adv.* **2014**, *4*, 71–75.

50 Yu, X.; Fan, H.; Liu, Y.; Shi, Z.; Jin, Z. *Langmuir* **2014**, *30,* 5497-5505.

51 Liebscher, J.; Mrówczyński, R.; Scheidt, H. a; Filip, C.; Hădade, N. D.; Turcu, R.; Bende, A.; Beck, S. *Langmuir* **2013**, *29* (33), 10539-10548.

52 Kinoshita, K. *Electrochemical Oxygen Technology*, 2nd ed.; Wiley: New York, 1992.

53 Bard, Allen J and Faulkner, L. R. *Electrochemical Method*, 2nd ed.; John Wiley & Sons: New York, NY, 2001.

54 Song, C.; Zhang, J. In *PEM Fuel Cell Electrocatalysts and Catalyst Layers*; Zhang, J., Ed.; Springer London, 2008.

55 Wang, X.; Lee, J. S.; Zhu, Q.; Liu, J.; Wang, Y.; Dai, S. *Chem. Mater.* **2010**, *22* (5), 2178–2180.

56 Ozaki, J.; Anahara, T.; Kimura, N.; Oya, A. *Carbon N. Y.* **2006**, *44* (15), 3358–3361.

57 Yang, W.; Fellinger, T-P.; Antonietti, M. *J. Am. Chem. SOC*. **2011**, *133*, 206-209.

58 Yang, Z.; Nie, H.; Chen, X.; Chen, X.; Huang, S. *J. Power Sources* **2013**, *236*, 238–249.

59 Shao, Y.; Wang, X.; Engelhard, M.; Wang, C.; Dai, S.; Liu, J.; Yang, Z.; Lin, Y. *J. Mater. Chem.* **2010**, *20*, 7491-7496.

60 Matter, P.; Zhang, L.; Ozkan, U. *J. Catal.* **2006**, *239* (1), 83–96.

61 Farjami, E.; Rottmayer, M. A.; Jay Deiner, L. *J. Mater. Chem. A* **2013**, *1*, 15501-15508.